A&A 623, A67 (2019)
https://doi.org/10.1051/0004-6361/201834204

Astronomy & Astrophysics

Deep X-ray view of the Class I YSO Elias 29 with *XMM-Newton* and *NuSTAR*⋆

I. Pillitteri[1,2], S. Sciortino[1], F. Reale[1,3], G. Micela[1], C. Argiroffi[3], E. Flaccomio[1], and B. Stelzer[4,1]

[1] INAF-Osservatorio Astronomico di Palermo, Piazza del Parlamento 1, 90134 Palermo, Italy
e-mail: ignazio.pillitteri@inaf.it
[2] Harvard-Smithsonian Center for Astrophysics, 60 Garden St., Cambridge, MA 02138, USA
[3] Università degli Studi di Palermo, Piazza del Parlamento 1, 90134 Palermo, Italy
[4] Eberhard Karls Universität, Institut für Astronomie und Astrophysik, Sand 1, 72076 Tübingen, Germany

Received 7 September 2018 / Accepted 22 January 2019

ABSTRACT

X-ray emission is a characteristic feature of young stellar objects (YSOs) and the result of the interplay between rotation, magnetism, and accretion. For this reason high energy phenomena are key elements to understand the process of star formation, the evolution of their circumstellar disks, and eventually the formation of planets. We investigated the X-ray characteristics of the Class I YSO Elias 29 with joint *XMM-Newton* and *NuSTAR* observations of total duration 300 ks and 450 ks, respectively. These are the first observations of a very young (<1 Myr) stellar object in a band encompassing simultaneously both soft and hard X-rays (0.3−10 keV in *XMM-Newton* and ≈3−80 keV in *NuSTAR*). The quiescent spectrum is well described by one thermal component at ∼4.2 keV absorbed by $N_{\rm H} \sim 5.5 \times 10^{22}$ cm^{-2}. In addition to the hot Fe complex at 6.7 keV, we observed fluorescent emission from Fe at ∼6.4 keV, confirming the previous findings. The line at 6.4 keV is detected during quiescent and flaring states and its flux is variable. The equivalent width is found varying in the range ≈0.15−0.5 keV. These values make unrealistic a simple model with a centrally illuminated disk and suggest a role of the cavity containing Elias 29 and possible reverberation processes that could occur in it. We observed two flares that have durations of 20 ks and 50 ks, respectively, and we observed the first flare with both *XMM-Newton* and *NuSTAR*. For this flare, we used its peak temperature and timing as diagnostics to infer a loop size of about 1−2 $R_\odot$ in length, which is about 20%–30% of the stellar radius. This implies a relatively compact structure. We systematically observed an increase in $N_{\rm H}$ of a factor five during the flares. This behavior has been observed during flares previously detected in Elias 29 with *XMM-Newton* and ASCA. The phenomenon suggests that the flaring regions could be buried under the accretion streams and at high stellar latitudes because the X-rays from flares pass through gas denser than the gas along the line of sight of the quiescent corona. In a different scenario, a contribution from scattered soft photons to the primary coronal emission could mimic a shallower $N_{\rm H}$ in the quiescent spectrum. In the spectrum of the full *NuSTAR* exposure, we detect hard X-ray emission in the band ≈20−80 keV which is in excess with respect to the thermal emission and that is significant at a level of ≥2σ. We speculate that the hard X-ray emission could be due to a population of energetic electrons accelerated by the magnetic field along the accretion streams. These particles, along with X-ray photons with $E > 7.11$ keV, could be responsible for pumping up the Fe fluorescence when hitting cold Fe in the circumstellar disk.

Key words. stars: activity – stars: coronae – stars: pre-main sequence – stars: formation – stars: flare

1. Introduction

X-ray observations of star-forming regions (SFRs) have established young stars as bright X-ray sources, from the Class I stage, when a thick envelope shrouds the central object; through Class II, when a thick disk has been fully formed and is visible; to the Class III stage, where very little, if any, circumstellar disk or envelope remains, the accretion process has ceased, proto-planets may have formed, and the photosphere of the disk-less star is hardly distinguishable from that of more mature stars (Montmerle et al. 1990; Feigelson & Montmerle 1999; Favata & Micela 2003)

Extensive and deep surveys of SFRs in X-rays have been obtained with *Chandra* and *XMM-Newton* (e.g., COUP, XEST, DROXO, CCCP, Getman et al. 2005; Güdel et al. 2007; Pillitteri et al. 2010; Townsley et al. 2011). From these data we assessed that a large fraction of the X-ray emission of Class I and II young stellar objects (YSOs) is of coronal origin as clearly shown, for example, by impulsive activity similar to the flares observed in the solar corona. The magnetic structures that form the stellar coronae of YSOs can sometimes create rotationally modulated emission (Flaccomio et al. 2005). Another component of the X-ray emission likely arises from the interaction of the central star and its circumstellar disk. This can be due to infalling matter heated by the accretion process (e.g., Kastner et al. 2002). Coronal activity affected by the accretion process has been proposed to explain the soft X-ray excess observed in young accreting stars (Güdel & Telleschi 2007). Another phenomenon is the fluorescent emission, mostly in the neutral Fe of the disk at 6.4 keV and likely stimulated by coronal X-rays with energies >7.11 keV (Imanishi et al. 2001; Tsujimoto et al. 2005). Imanishi et al. (2001) detected a prominent Fe Kα line at 6.4 keV in a *Chandra* spectrum, for the first time, during a large flare in the YSO YLW16A, which is located in the ρ Ophiuchi Dark Cloud. These authors explained the feature as the result of the excitation of neutral Fe from hard X-ray photons produced during the flare. In the spectra obtained with a continuous ACIS observation of 850 ksec dubbed the *Chandra* Orion Ultradeep Project (COUP), Tsujimoto et al. (2005) reported the detection

⋆ Based on observations obtained with *XMM-Newton*, an ESA science mission with instruments and contributions directly funded by ESA member states and NASA

of a Fe Kα 6.4 keV line in 7 flaring sources in Orion. The 500 ks Deep ρ Oph *XMM-Newton* Observation (DROXO) of the core F region revealed 61 ρ Ophiuchi YSO members (Pillitteri et al. 2010). In 9 of these 61 YSOs, specifically in 4 Class I, 4 Class II, and 1 Class III objects, Stelzer et al. (2011) detected the Fe Kα 6.4 keV line both during flaring and quiescent phases.

Using a novel Bayesian method, Czesla & Schmitt (2010) reanalyzed the COUP data and found the Fe Kα 6.4 keV line in 23 out of 106 YSOs in the Orion Nebula. From these results we can infer that fluorescence occurs more frequently than previously thought. In some cases the emission is associated with soft X-ray flares, but it sometimes appears as a steadily persistent feature, even during quiescent periods.

Elias 29 is a Class I/II YSO in the Rho Oph Dark Cloud, where Giardino et al. (2007; hereafter Paper I) detected significant variability in the equivalent width (EW) of the Fe Kα 6.4 keV line during the DROXO observation. The 6.4 keV line was weak, but present, during the first quiescent time interval (cf. Fig. 4 of Paper I, EW $\sim$ 30 eV) and appeared at its maximum strength 90 ks after Elias 29 underwent a flare with an EW $\sim$ 800 eV. The thermal X-ray emission was the same in the two time intervals, while variability of the 6.4 keV line was significant at a 99.9% confidence level.

As for excitation mechanisms, photoionization alone could not be sufficient to explain strong fluorescent emission with EW in excess of ~150 eV; other mechanisms such as collisional excitation are also invoked. Drake et al. (2008) analyzed the Fe Kα fluorescent line emission in a few stars concluding that there was not compelling evidence for a collisionally excited fluorescence from high energy electrons. On the one hand a simple disk illuminated geometry cannot produce EW in excess of 150 eV and thus the origin of the strong emission observed in Elias 29 is still not clear. More generally, Drake et al. (2008) considered four different possible explanations for the case of Fe Kα with EW > 150 eV, namely: (1) high Fe abundance of the disk material that could increase line intensity, but which rapidly saturates at EW $\sim$ 800 eV (Ballantyne et al. 2002); (2) disk flaring that, thanks to favorable geometry, can increase line intensity by a factor two or three; (3) emission induced by an "unseen" flare obscured by the stellar disk implying that the evaluation of the exciting continuum is grossly underestimated; and (4) excitation due to high energy non-thermal electrons, which nonetheless requires a substantial amount of energy stored in the impinging particles (Ballantyne & Fabian 2003). Since the presence of the Fe Kα fluorescent line with EW > 150 eV is a very common feature among YSOs, explanations based on ad hoc geometry of the system or peculiar conditions of the systems still seem unsatisfactory. The extraordinary example of Fe fluorescence of V 1486 Ori (Czesla & Schmitt 2007), where an EW of ~1400 eV has been measured, can be explained only recurring to an excitation from highly energetic particles. We note however that fluorescent Fe emission at ~6.4 keV is also observed in active galactic nuclei (AGN); in these sources, similar to what happens in young stars, a central X-ray source illuminates the cold material located in the surrounding torus/disk system. There large EW (0.2 < EW < 2 keV) are often observed, especially for sources with $N_{\rm H} > 10^{23}$ cm^{-2} (e.g., Fukazawa et al. 2011). The soft (0.3–10 keV) and hard (>10 keV) X-ray spectra of a YSO with a disk showing Fe fluorescence can reveal the presence of a non-thermal population of electrons responsible for at least part of the fluorescence. In this context we obtained a joint and simultaneous *XMM-Newton* and *NuSTAR* observation of Elias 29 devoted to acquiring spectra from soft (*XMM-Newton* band 0.3–8.0 keV) to hard (*NuSTAR* band 3–80 keV) X-rays. We conceived this program to detect any non-thermal hard X-ray emission from Elias 29, study the time variability, and relate these features to the fluorescent emission, and eventually explain its origin.

We present the characteristics of the new X-ray observations and the adopted analysis in Sect. 2, we illustrate the results of the time-resolved spectral analysis in Sect. 3, discuss the results in Sect. 4, and finally we draw our conclusions in Sect. 5.

Table 1. Log of the observations.

Satellite	ObsID	Start (UT)	Net exposure (ks)
XMM-Newton	0800030801 (First)	2017-08-13T16:34:58	99.65
XMM-Newton	0800030901 (Second)	2017-08-15T16:26:29	100.11
XMM-Newton	0800031001 (Third)	2017-08-17T19:26:33	95.02
NuSTAR	30301001002 (First)	2017-08-13T14:36:09	55.34
NuSTAR	30301001004 (Second)	2017-08-15T14:56:09	94.24
NuSTAR	30301001006 (Third)	2018-06-15T16:06:09	102.3

Notes. We refer to the *XMM-Newton* observations as first, second, and third *XMM-Newton* observation, respectively. Analogously we refer to the first, second, and third *NuSTAR* observation for simplicity. For *NuSTAR* the science time per orbit is about 55% of the orbit duration. The third *NuSTAR* observation was obtained about 10 months after the joint *XMM-Newton* and *NuSTAR* observations.

2. Observations and data analysis

Elias 29 ($\alpha = 16^{\rm h}27^{\rm m}09.4^{\rm s}$, $\delta = -24^{\rm d}37^{\rm m}18.9^{\rm s}$; other identifiers: [GY92] 214, 2MASS J16270943-2437187, ISO-Oph 108) is the most IR luminous Class I YSO in the Rho Ophiuchi Dark Cloud (Bontemps et al. 2001; Natta et al. 2006). The accretion rate of this YSO is about $1.5 \times 10^{-6}\,M_\odot\,{\rm yr}^{-1}$; its circumstellar disk has an estimated mass of about 0.012 $M_\odot$; its inner radius is ~0.36 AU, which is about 13 stellar radii ($R_\star \sim 5.7$–$5.9\,R_\odot$); and the outer radius of the disk is about 600 AU (Boogert et al. 2002; Miotello et al. 2014; Rocha & Pilling 2015). The system is tilted in such a way that the line of sight partly crosses the envelope, and the star is visible through the outflow cavity and a portion of the disk (cf. Fig. 14 in Rocha & Pilling 2015).

The *XMM-Newton* and *NuSTAR* observations were acquired as part of a large, joint program (PI: S. Sciortino). The total exposure time was ~300 ks for *XMM-Newton* and ~450 ks for *NuSTAR*; however about 250 ks of science exposure were obtained with *NuSTAR* because of the low orbit of this telescope. The surveyed region covered most of the dense core F of LDN 1688 that is approximately 6′ north of the previous pointing of the 500 ks *XMM-Newton* observation known as DROXO (Pillitteri et al. 2010). Basic information on the *XMM-Newton* and *NuSTAR* observations are reported in Table 1.

2.1. XMM-Newton observations

The three *XMM-Newton* observations were carried out on three subsequent satellite orbits (orbits 3238 to 3240), with a nomimal aim point at Elias 29 and very little variation of the position angle among the three orbits. We refer to the *XMM-Newton* observations as the first, second, and third *XMM-Newton* observation, respectively. A log of the observations is reported in Table 1. The *XMM-Newton* EPIC ODF data were processed with SAS software[1] (version 16.1.0) and the latest calibration files to produce full field of view (FOV) lists of events calibrated in both energy and astrometry (Fig. 1).

[1] See http://xmm.vilspa.esa.es/sas

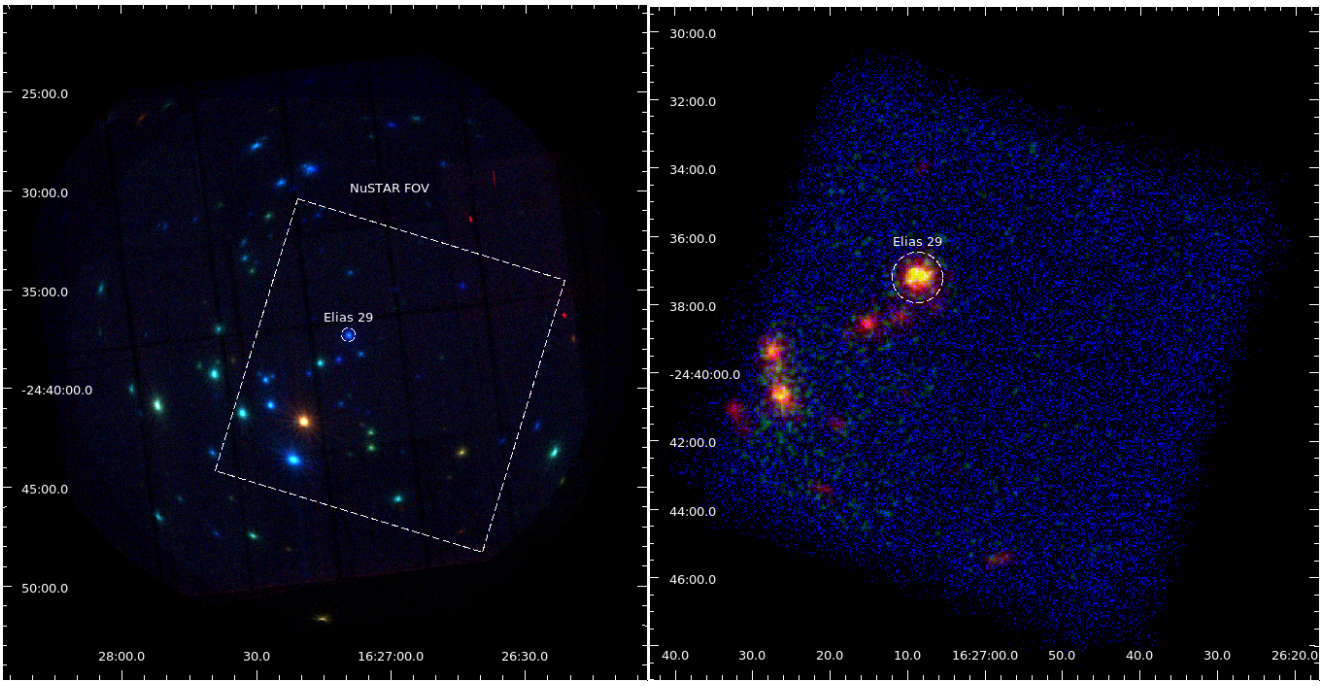

Fig. 1. *Left panel*: color-coded image of the EPIC data integrated over the entire observation (red: 0.3−1.0 keV; green: 1.0−3.0 keV; blue: 3.0−8.0 keV). The square indicates the FOV of the *NuSTAR* observation. *Right panel*: color-coded image of the *NuSTAR* data integrated over the entire observation (red: 3−10 keV; green 10−40 keV; blue 40−60 keV). In both images a circle indicates the position of Elias 29.

We subsequently filtered these photons and retained only those with energy in the 0.3−8 keV band and only the events that triggered at most two nearby pixels simultaneously (FLAG==0; PATTERN ≤ 12). This filtering was operated on the data of each EPIC detector (MOS1, MOS2, PN) for each of the exposure segments of the three *XMM-Newton* observations. The chosen energy band limits ensure a good overlap with the *NuSTAR* band and the best EPIC calibration.

High background variability was present during the first part of each *XMM-Newton* exposure. This has the effect of increasing the noise in light curves and spectra when subtracting the background. However, for Elias 29 we preferred to use the full exposure time rather than excising the intervals with high background to ensure continuous monitoring. We used a circular region of radius 30″ centered on the source centroid to extract the events for both MOS and PN. This region should contain about 80% of the encircled energy of the *XMM-Newton* point spread function (PSF).

The background events were extracted from a nearby circular region of 40″ radius without sources from the same chip and, for the PN, at the same distance from the read-out node, as prescribed by the SAS guide. In order to produce the spectra we used a more strict selection (PATTERN ≤ 4) as recommended in the SAS guide. With SAS we obtained light curves and spectra for source and background events, response matrices (RMF), and effective area files (ARF) for the spectral analysis. The spectra were grouped to have at least 25 counts per bin before analysis with the XSPEC software.

2.2. NuSTAR *observations*

Two *NuSTAR* observations were taken simultaneously with the *XMM-Newton* observations, while a third exposure of duration ∼195 ks was obtained in June 2018. This third exposure without an *XMM-Newton* counterpart was not initially planned as part of the campaign. Owing to the low satellite orbit, the total science exposure amounts to ∼250 ks out of a total exposure of ∼450 ks.

The *NuSTAR* data were processed with the HEASOFT suite (version 6.22.1), the *NuSTAR* dedicated pipeline, and the latest calibration files (CALDB ver. 4.8) to produce full FOV lists of events calibrated in both energy and astrometry for the two cameras FPMA and FPMB. The resulting image in the 3−60 keV band is shown in Fig. 1 (right panel) where about ten sources are recognized by eye. The sources in the FOV are rather weak, and Elias 29 is the strongest.

We adopted the standard thresholds for the rejection of particle background and the cutoff threshold at the SAA passage. For Elias 29 we extracted the spectra from a circular region with a radius of 40″centered on the source centroid; this region should contain about 40% of the total source counts (Harrison et al. 2013). A circular area of 80″ radius was used to extract the background events from a nearby region. The tasks NUPRODUCTS and NUPIPELINE were used to extract events in different energy bands and time intervals and to create spectra, light curves, and related calibration files such as response matrices and ARF for the spectral analysis with XSPEC.

2.3. Spectral analysis

Spectra from the events of *XMM-Newton* MOS1, MOS2, and PN and *NuSTAR* FPM A and B were accumulated in different time intervals for time-resolved spectroscopy (see Sect. 3.2). The spectra (energy band 0.3–8.0 keV) were modeled with an absorbed thermal APEC component to derive the properties of the emitting plasma, specifically the temperature, emission measure (EM), global abundances ($Z/Z_\odot$), and flux. In addition, we used a Gaussian line with intrinsic width equal to zero to model the fluorescent emission in the 6.4−6.6 keV range[2]. The EPIC spectral resolution is the main factor of the broadening of the Gaussian line width. In principle we could expect a variation of

[2] In XSPEC terminology TBabs(APEC+Gaussian).

the lines contributing to the blend of fluorescent emission and their relative strengths, however we do not expect velocity fields that can increase the line width to a detectable level. The global abundance was derived from the best-fit modeling to the spectrum of the third *XMM-Newton* observation (ObsID 080031001) with a value $Z/Z_\odot = 0.54$. This is consistent with subsolar $Z/Z_\odot$ often derived from the analysis of low resolution spectra of young coronae (Maggio et al. 2000; Güdel 2003; Maggio et al. 2007). For the other time intervals we used a fixed $Z/Z_\odot = 0.54$.

The results of this analysis are presented in Table A.1. Overall, the spectrum of Elias 29 is smooth and the only prominent feature is the Fe xxv line at 6.7 keV, due to the high temperature of the corona, and the neutral Fe line at 6.4 keV from the fluorescence. The blend between the 6.7 keV Fe line and the fluorescent line at ~6.4 keV requires a careful estimate of the APEC abundance and the temperature to avoid biases in the line centroid and strength of the 6.4 keV line. The determination of the centroid position and the Gaussian EW are affected by the low spectral resolution of EPIC, limited count statistics of the spectra, strength of the line, as well as by gas absorption, temperature, and Fe abundance for the estimate of the continuum and the blend with the 6.7 keV line. For this reason we also performed a best-fit modeling to the spectra in the energy range 5−8 keV. In this narrower band the value of $N_{\rm H}$ absorption is less constrained, however the continuum of the line is determined by the APEC temperature and its normalization, and the abundance value $Z/Z_\odot$ constrains the intensity of the 6.7 keV Fe line. The best-fit value of the temperature found in the full band produces an acceptable fit in the narrow band. However only for the purpose of the best evaluation of the continuum around 6.4 keV we let free to vary the temperature and global abundances. The results from such fits are listed in Table A.3 and we refer to these results when we discuss the fluorescence (Sect. 3.4). The $N_{\rm H}$ value was kept fixed to the value estimated from the quiescent level ($N_{\rm H} = 5.5 \times 10^{22}$ cm^{-2}). Approximately, half of the counts in the full band spectrum are present in the 5–8 keV band. For the first and third *XMM-Newton* observations (ObsID 08030801 and 08031001) we considered the full exposure to keep an adequate level of count statistics, while for the second observation (ObsId 08030901) we analyzed the spectra in the same time intervals used for the full energy band. The choice of the time intervals is detailed in Sect. 3.2.

3. Results

Visual inspection of the *XMM-Newton* images shows the presence of more than 100 sources, while in the smaller *NuSTAR* FOV we can easily recognize about 10 sources. We defer the study of the remaining X-ray sources to a separate paper, while in this paper we focus on Elias 29, which is the strongest of the *NuSTAR* sources (cf. Fig. 1).

3.1. *XMM-Newton* and NuSTAR light curves of Elias 29

The PN and FPM light curves or Elias 29 are shown in Fig. 2. Two major flares occurred during the exposures, but only the first flare was observed simultaneously with *XMM-Newton* and *NuSTAR*. The first flare had a duration of about 20 ks and an exponential decay time of about 7.6 ks, and the second flare had a duration of about 50 ks with an exponential decay time of about 9.3 ks. Before the second flare, it is possible that the final decay of another flare was recorded with *NuSTAR*. The lack of *XMM-Newton* simultaneous coverage limits the information we can obtain about the second flare, however its detection allows us to infer that approximately every 200–250 ks a flare of intensity similar to those observed in the present data can occur on Elias 29. A detailed analysis of the first flare is given in Sect. 3.2.3. Other than the two main flares, we notice that in the first *XMM-Newton* observation (ObsID 080003081) the rate smoothly increased and then decreased on a timescale of about 50 ks; it also showed a very short spike in the same time interval.

In order to study the time variability and identify any statistical change in the count rate, we compared two distinct techniques: the Bayesian change point (bcp) analysis[3] (Wang & Emerson 2015; Erdman & Emerson 2007, 2008) and the Prune Exact Linear Time (PELT) analysis[4] (Killick et al. 2012). The first method (bcp) uses a Bayesian approach to determine the change points in a time series. For each data point this method derives a posterior mean of the rate and a probability of change of the rate at each data point. The second method, PELT, uses a competitive algorithm that minimizes a cost function while guarding against overfitting the data by means of a penalty function. Figure 3 shows the posterior mean and posterior probability of a change at each light curve bin obtained from the *bcp* analysis. In the probability panel we can decide which threshold to use to identify variability at some level of significance. For example, we can pick the values at $P = 0.3$ and $P = 0.1$, respectively. Above $P = 0.3$ we can decide that there is a change of the rate, while between $P = 0.1$ and $P = 0.3$ we could have a likely change of the rate. Similar results are obtained for *NuSTAR* light curves, however the lower count statistics of the data introduces more spurious peaks of posterior probability above 0.3 that do not look related to real variability.

Figures 4 and 5 show the results from PELT analysis: the input background-subtracted PN and FPM light curves are shown with overplotted the time segments and individual segment average rate. We identified change points based on changes of mean rate and its variance (*cpt.meanvar* function). We used an asymptotic type penalty and the default value of 0.05 (corresponding to a 95% statistical significance level at each change point). We further checked the results of the number of intervals identified by using a "manual" value for the penalty function and producing a plot of the number of change points as a function of the penalty[5]. Small values of the penalty produce more spurious change points, and their number flattens out rapidly with increasing values of the penalty. The "elbow" corresponds to the number of expected change points. Compared to bcp PELT seems less sensible to small variations of the rate while bcp analysis seems more capable of finding short duration change of rate of smaller amplitude. On the other hand, the time segments found with PELT are more adequate for performing a robust time-resolved spectral analysis as they include more counts overall. We performed the same analysis on the narrow energy band of 6.1−6.9 keV around the complex of the Fe lines at 6.4−6.7 keV. We obtained four intervals that identify the pre- and post-flare quiescent level, a flare peak segment, and a flare decay segment in agreement with the full energy band analysis. For the time-resolved spectroscopy we used the time segments identified with PELT on the light curve of the full energy band of *XMM-Newton* (0.3–8.0 keV). The total net counts in the different intervals vary between ~600 and ~3400 (cf. Table A.1).

[3] Implemented in the *R* package "bcp".
[4] Implemented in the *R* package "changepoint".
[5] See, e.g., www.stats.stackexchange.com/questions/60245/penalty-value-in-changepoint-analysis/60440#60440

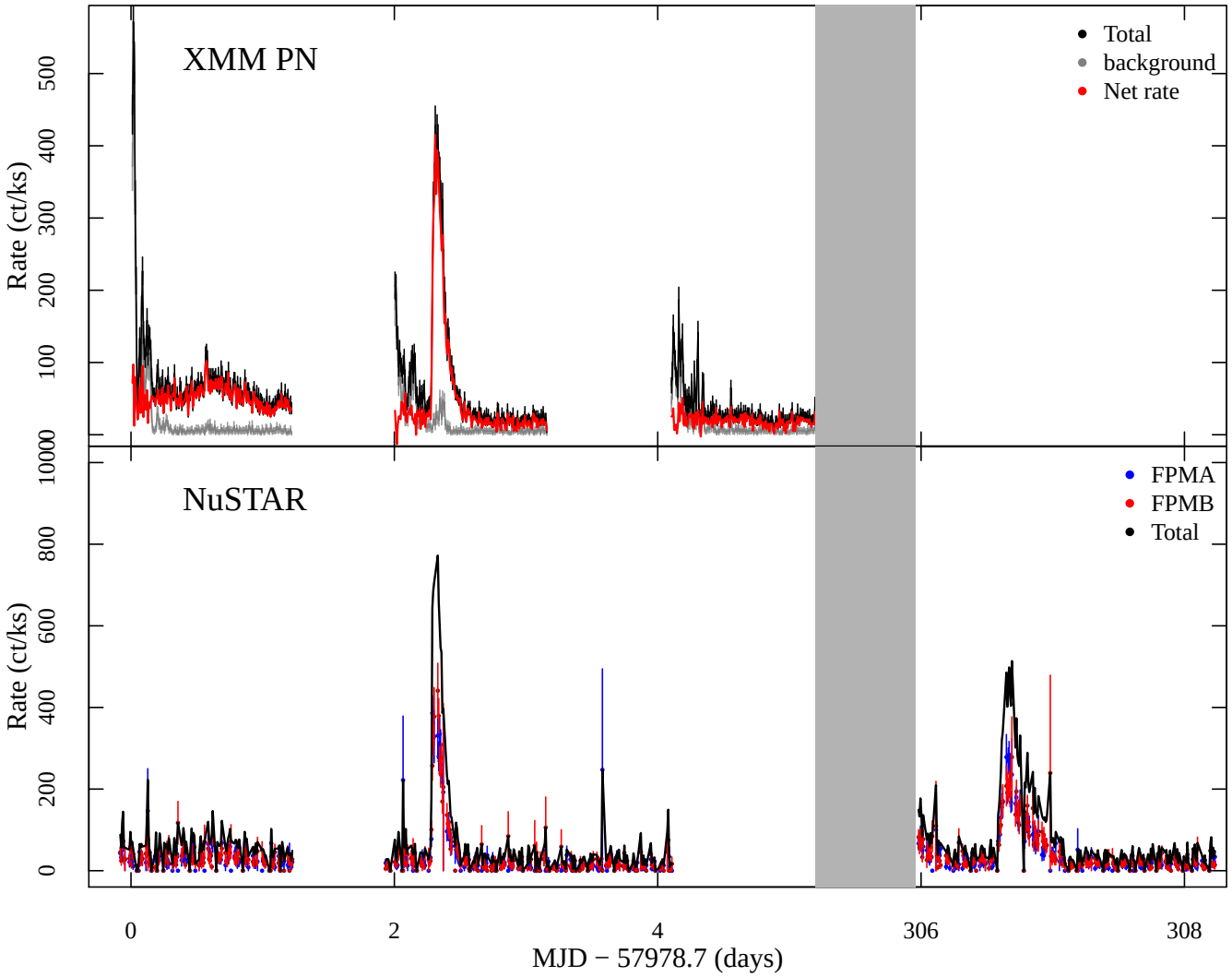

Fig. 2. *XMM-Newton* PN (*top panel*) and *NuSTAR* (*bottom panel*) light curves of Elias 29. High background variability affects the first part of each *XMM-Newton* exposure and during the main flare, but its effect can be adequately corrected as shown by the background-subtracted (red) light curve. The origin of time axes is set to the time of start of the first PN exposure. The time gap between the second and third *NuSTAR* exposures is indicated with the gray area and amounts to about 300 days.

The light curve of the third *NuSTAR* exposure is divided into five segments by PELT. We can recognize an initial partial decay phase, likely from an unseen flare, and then a quiescent segment before the flare, a peak, and a decay segment for the flare and post-flare quiescent phase.

3.2. XMM-Newton time-resolved spectroscopy

3.2.1. Quiescent emission

The third *XMM-Newton* observation shows a low PN rate for about 100 ks, and it appears as a continued quiescent phase after the flare registered in the second *XMM-Newton* exposure. Despite PELT identifies two time intervals with different rate variance during the third exposure, we considered the full exposure as a whole for producing the MOS and PN spectra. The PN spectrum is shown in Fig. 6 with the best-fit model composed by an APEC plus Gaussian line. The best-fit parameters of the model are shown in Table A.1. The average plasma temperature is ~4 keV (90% confidence range 3.1−5.6 keV) and the hydrogen column density $N_{\rm H}$ is 5.5×10^{22} cm^{-2} (90% confidence range $3.1-5.6 \times 10^{22}$ cm^{-2}). These values are similar to those found by Giardino et al. (2007) and by Favata et al. (2005), and thus we conclude that the X-ray coronal emission of Elias 29 has been stably hot over a timescale of ~12 yr. The quiescent unabsorbed flux in 0.3−8.0 keV is about 6.3×10^{-13} erg s^{-1} cm^{-2} , which corresponds to $L_{\rm X} \sim 1.1 \times 10^{30}$ erg s^{-1} at 120 pc.

Furthermore, we accumulated a PN spectrum of the exposure encompassing the quiescent period after the flare in the second *XMM-Newton* exposure (segment 5) and the whole third exposure. This is justified by the similar count rate in both segments that suggests similar spectral characteristics of the plasma. The resulting PN spectrum had about 3400 counts, the best fit with an absorbed APEC component had the following values (90% confidence range in braces): $N_{\rm H} = 5.8\,(5.3-6.4) \times 10^{22}$ cm^{-2}, $kT = 4.2\,(3.6-5.3)$ keV, $Z/Z_{\odot} = 0.6\,(0.4-0.8)$, $\log {\rm EM} = 52.78\,(52.77-52.79)$ cm^{-3}, and unabsorbed flux in 0.3−8 keV band $\log F_{\rm APEC} = -12.21$ (−12.23 − −12.19) erg s^{-1} cm^{-2} (see Table A.1). Fluorescence is firmly detected in the quiescent phase, as the modeling of the quiescent spectrum with a thermal APEC component alone shows a sharp excess of emission around 6.4–6.5 keV (Fig. 6). The Gaussian line gives a best-fit centroid of 6.49 (6.40−6.60) keV, EW = 0.25 (0.16−0.38) keV and flux of the line of $\log F_{\rm Gau} = -14.17$ (−14.27 − −13.93) erg s^{-1} cm^{-2}.

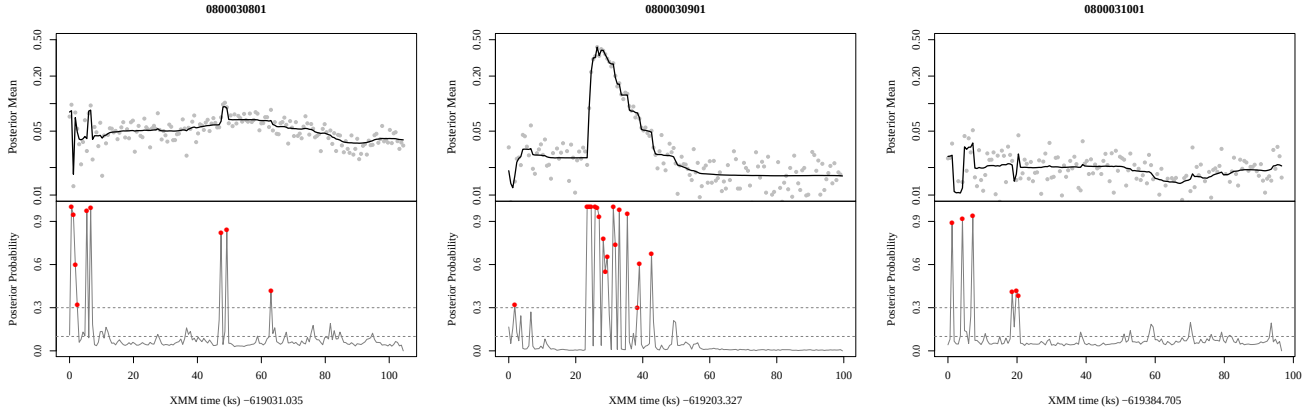

Fig. 3. Analysis via BCP of the *XMM-Newton* PN light curves in the 0.3–8.0 keV bandpass. *Top panel*: light curve (gray dots) with the posterior mean (solid line). The scale of the y-axis is logarithmic and with the same range of values across the 3 panels for ease of comparison. *Bottom panel*: posterior probability at each point. We indicated the probabilities $P > 0.3$ with red dots; the horizontal dotted lines show the levels at significance $P = 0.3$ and $P = 0.1$, respectively.

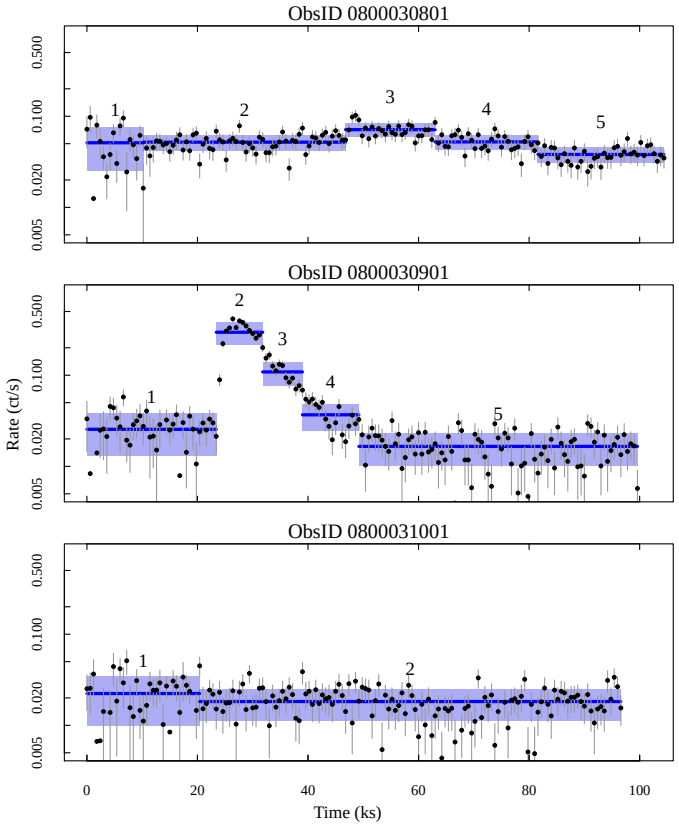

Fig. 4. Analysis via PELT of the *XMM-Newton* PN light curves in the 0.3–8.0 keV bandpass subtracted of background rate. Bin size is 600 s and the rate is shown in a log scale. Panels have the same range on the y-axis. Horizontal segments and shaded areas indicate the average count rate and variance in each time interval (numbers on top of the intervals). The semi-log scale helps to recognize the regular exponential decay of the flare.

3.2.2. Smooth variability

In the first *XMM-Newton* observation (ObsID 0800030801) the PN rate of Elias 29 showed a slow increase of the rate followed by a similar smooth decrease. A spike of duration ≤2 ks is visible near the center of the exposure, and aside from this spike there is no evidence of other rapid variability. Following the subdivision in time intervals from PELT we performed time-resolved spectroscopy in each of the resulting five intervals with models as described in Sect. 2. The best-fit values of the $N_{\rm H}$ gas absorption vary in the range $5.4{-}7.2 \times 10^{22}$ cm^{-2} within the five segments, however these values are still consistent with each other and with the $N_{\rm H}$ derived from the quiescent spectrum at a 90% confidence level. The best-fit temperature, kT, varies in the 3.4−5.4 keV range during the first observation, however kT value is still consistent with the quiescent temperature derived from the last *XMM-Newton* observation at a confidence level of 90%. Also, the segment that contains the short spike has a somewhat high temperature (5.4 keV, 90% range ∼4.2−6.9 keV).

In Fig. 7 we show the average spectrum of the whole first exposure of *XMM-Newton* observation compared to the average spectrum of the last exposure, which represents the quiescent emission. The gas absorption $N_{\rm H}$ and plasma temperature kT were found to be similar in the two spectra at $N_{\rm H} \sim 5.5{-}6.5 \times 10^{22}$ cm^{-2} and $kT \sim 4{-}4.2$ keV, respectively. The EM was found to be larger by a factor of three during the first observation with respect to the EM of the third (quiescent) observation.

The smooth variability occurred on a timescale of less than one day and was not observed again in the following exposures. We speculate that the increase of rate could have been caused by an active coronal region appearing on view because of the stellar rotation. Such a region would contain plasma that is denser than the rest of the corona, thus resulting in an increase of the EM. In addition, the region could show flaring activity such as the short spike we observed, as a result of the complex dynamics of the magnetic structures in it. The passage of such a region lasted about 80 ks or ∼0.93 days; this is consistent with a rotation period of about two days, which is typical of a very young Class I YSO like Elias 29. The fact that it did not appear again in the second *XMM-Newton* exposure sets a lifetime to the order of one day. However, the region itself could have hosted the main flare observed in the second exposure when the region appeared in view again. The flare could have also destroyed or heavily reshaped the active region as this latter did not appear again in the third *XMM-Newton* observation.

3.2.3. Flare analysis

Two main flares were observed in Elias 29 but we discuss the first flare in depth because of the simultaneous coverage with *XMM-Newton* and *NuSTAR* coverage. This flare showed a very

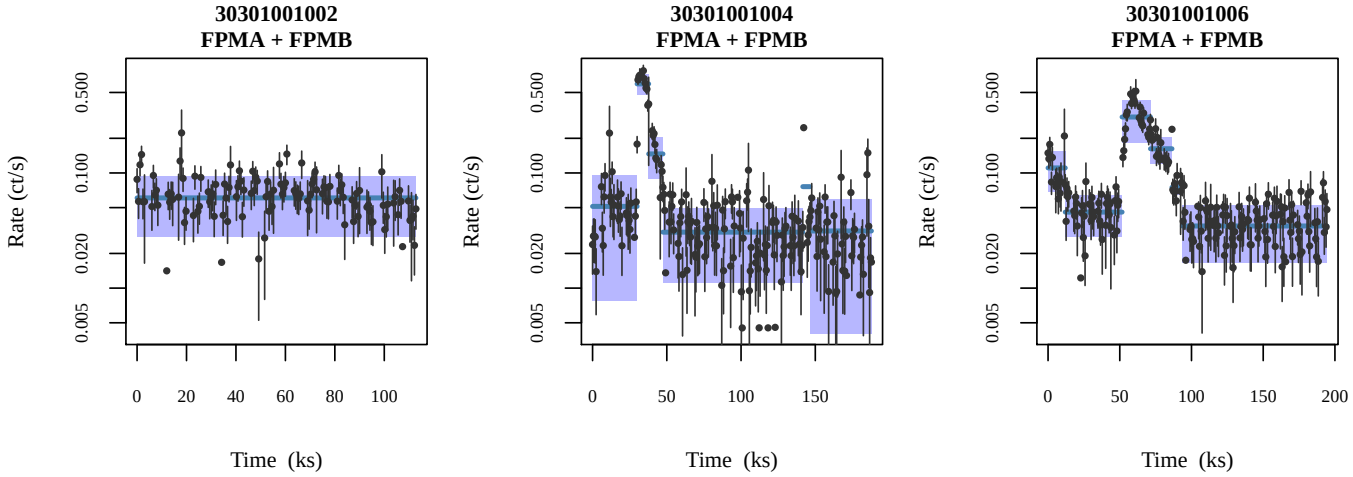

Fig. 5. As in Fig. 4 for *NuSTAR* light curves in the 3−80 keV.

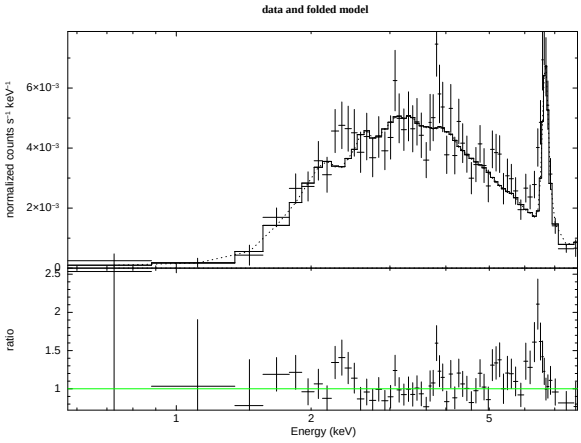

Fig. 6. Spectrum of the PN during the quiescent phase (*top panel*) and ratio data/model. The spectrum was accumulated from events collected during the quiescent phases after the flare and in the third *XMM-Newton* observation. The model is an absorbed APEC thermal component. A sharp excess of emission is visible at ∼6.4 keV and due to the fluorescent emission present even during quiescence.

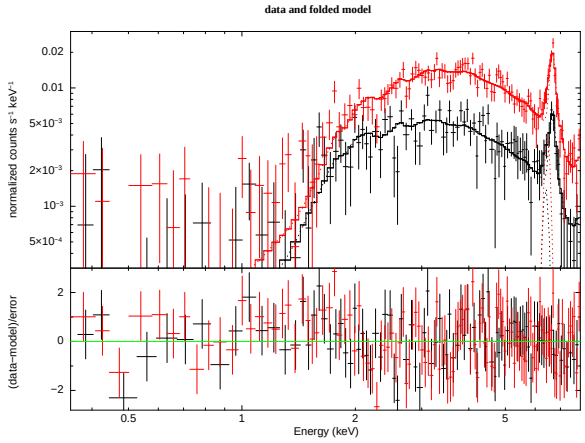

Fig. 7. Spectra and best-fit models of the PN detector acquired during the first *XMM-Newton* exposure (red symbols) and the third exposure (black symbols). *Lower panel*: residuals (data – model values). The model for both spectra is an absorbed thermal APEC component plus a Gaussian to take into account the fluorescent emission from partially ionized Fe lines at 6.4−6.5 keV. The difference between the two spectra is due to a difference of EM.

regular decay phase well modeled with an exponential decay. The decay of the flare appears faster in the hard band (5–8 keV) than in the soft band (0.3–5.0 keV); e-folding times are $\tau_0 \sim 4.1$ ks in the hard band and $\tau_0 \sim 7.6$ ks in the soft band (Fig. 8). A similar timing is observed in *NuSTAR* data with a decay time equal to $\sim 4.2 \pm 0.5$ ks and a rise time of $\sim 1.8 \pm 0.6$ ks. The light curve of the PN shows a peak rate ≈8 times the quiescent rate before the flare rise and has a peak luminosity $\log L_X = 31.18$. The duration and luminosity of this flare are larger than those of solar flares (e.g., Tsuboi et al. 2016) but not exceptional when compared to some of the flares observed in YSOs of the Orion Nebula (Favata et al. 2005; Caramazza et al. 2007; Wolk et al. 2005) and in ρ Ophiuchi itself (Pillitteri et al. 2010). A flare with similar duration and peak rate was observed by Giardino et al. (2007). Taking into account the past X-ray observations, in a total exposure time of ∼800 ks Elias 29 has shown flares with duration of less than one day and peak rate about ten times the quiescent rate. The second flare, observed only with *NuSTAR*, had total duration of about 50 ks (almost 14 h), which is substantially shorter than the day long-lasting flares were seen in the Orion Nebula and in ρ Ophiuchi.

The modest brightness of the flare implies a modest count statistics. This fact reduces the detail and accuracy of the time-resolved spectroscopy we can perform on it. The PELT algorithm divided the flare roughly in a peak segment (number 2), two decay segments (marked 3 and 4), and two quiescent segments (1 and 5) before and after the flare, respectively. Table A.1 lists the best-fit parameters of the flare segments. In order to improve the statistics and better constrain the model parameters, we made a simultaneous fit of the spectra of segments 1 and 5 as they are representative of the quiescent phases before and after the flare. In these time intervals we measured $N_H \sim 7 \times 10^{22}$ cm^{-2}, $kT \sim 5.9$ keV, log EM ∼ 52.8, and an unabsorbed flux log $Flux \sim -12.19$, which are similar to the values obtained from the spectrum of the quiescent phase of the third *XMM-Newton* exposure.

During the flare there is an increase of both the temperature and gas absorption. The temperature rises to about 11.1 keV (∼130 MK) and the absorption reaches values of $N_H \sim 2.1 \times 10^{23}$ cm^{-2}, which is about a factor of four higher than the N_H of the quiescent phase. The difference of N_H between

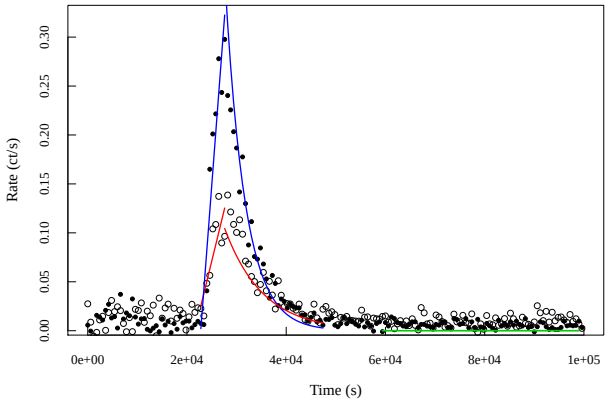

Fig. 8. *XMM-Newton* PN light curves in the 0.3−5.0 keV (open circles) and 5−8 keV (solid dots) with the best fit of the rise phase (linear increase) and decay phase (exponential decrease). The rates are subtracted from the respective background rates. The green segment indicates the interval where the median of the quiescent rate has been calculated. The quiescent rate has been subtracted to derive the decay times.

quiescence and flare states is significant at a level $> 3\sigma$. A similar increase of $N_{\rm H}$ was noticed by Giardino et al. (2007) in the flare observed in DROXO and by Kamata et al. (1997) in a flare observed with ASCA. Such a behavior suggests that the X-rays from the flaring region cross material optically thicker than the gas crossed by X-rays coming from the quiescent corona. Kamata et al. (1997) attributed the increase of $N_{\rm H}$ to the disk and envelope geometry surrounding Elias 29. They proposed that the flaring sites are preferentially at a low latitudes and their lines of sight cross the disk. This explanation however remains at odds with the face-on geometry of the disk inferred from far-infrared observations (cf. Boogert et al. 2002).

We remark that the flare temperature peaks at segment 2, but the EM is detected at its maximum during segment 3. The time delay between the temperature and the EM peaks is predicted by models of flaring loops (e.g., Reale 2007): the flare heat pulse drives a strong plasma flow from the chromosphere upward along the magnetic tube, and the flow continues to fill the tube for some time after that the heat pulse has stopped (and the cooling starts). It is then reasonable to work in the assumption that the flare occurs in a single flaring loop, and to use the related diagnostics to determine the characteristics of the flaring loop based on hydrodynamic simulations and calibrations on X-ray solar flare observations (Reale 2007). In particular, we may infer the semi-length of the loop L from the decay time of the flare, peak temperature, and slope of the decay in the density-temperature diagram using Eqs. (A.1)–(A.3) in Reale (2007). We derive a maximum temperature at the peak of ∼325 MK from the kT at segment 2 (11.1 keV ∼130 MK) and log EM[cm^{-3}] ∼ 54.24. Because of the large uncertainties in the temperature we cannot derive a reliable value of the slope in the density-temperature diagram. Thus, we assumed the maximum value of the slope determined by Reale (2007). The maximum slope corresponds to the case of absent sustained heating during the flare decay, i.e., consistent with the pure cooling of a single flaring loop. A shallower curve in the density-temperature diagram would instead suggest the progressive involvement of more and shorter loops, as in arcade flares. Our assumption implies that we are deriving an upper limit for the length L of the flaring loop(s). We measure an e-folding decay time $\tau \sim 7.65$ ks from the light curve in the soft band 0.3–5 keV (Fig. 8) and we estimate $L \leq 2.0 \times 10^{11}$ cm or $L \leq< 2.9\,R_\odot$ (or <0.5 stellar radii).

Keeping the same assumption an alternative estimate can be derived from the rise phase, as described in Reale (2007), and in particular from Eq. (12) therein

$$L \approx 10^9 \psi^2 T^{1/2} \Delta t_{\rm R}, \quad (1)$$

where L is in cm, $T = 332$ MK is the loop maximum temperature at the flare peak, and $\Delta t_{\rm R}$, in ks, is the time range between the flare start and its peak; we assume that the peak of the light curve is a good proxy of the EM peak. From the light curve we measure $\Delta t_{\rm R} = 3 \pm 0.3$ ks. The factor ψ is the ratio of the maximum temperature to the temperature at the density maximum. This is unconstrained in our case, and the whole possible range $1.2 < \psi < 2$ reported in Reale (2007) is the best we can take for the estimate. From Eq. (1) we obtain a range $0.5 \times 10^{11} < L < 1.3 \times 10^{11}$ cm, i.e, $0.7\,R_\odot < L < 1.8\,R_\odot$ (still $L < 0.3$ stellar radii), which is consistent with the upper limit from the decay time but more stringent.

The energy of the flare is estimated by integrating the luminosity during the flare and it is about 8×10^{34} erg released in about 20 ks. Still in the framework of a single flaring structure, and assuming a representative semi-length $L \approx 10^{11}$ cm (∼1.5 $R_\odot$), which is a typical cross-section radius of $R_L = 0.1L$ (see, e.g., Golub et al. 1980 and Klimchuk et al. 2000), and considering the values of EM derived from the spectral analysis, we can push our analysis to infer a value of the electron density in the loop during the flare from EM $\sim n_{\rm e}^2 V$, where $V = 2\pi R_L^2 L$ is the total volume of the loop. Although this is to be taken with care, for a peak value of EM $\sim 2 \times 10^{54}$ cm^{-3} and $V \sim 6 \times 10^{31}$ cm^3 we obtain $n_{\rm e} \sim 2 \times 10^{11}$ cm^{-3}, which is similar to the typical values found for solar flaring loops (e.g., Reale 2014).

From the density and temperature, we can in turn infer a minimum strength of the magnetic field (B_0) that is capable of confining the plasma inside the loop (e.g., Maggio et al. 2000); this is on the order of $B \geq B_0 = (16\pi n_{\rm e} k_{\rm B} T)^{1/2} \sim 500$ G, which is similar to other flares of active stars and compatible with average fields of kG on the stellar surface, as found in other YSOs.

For the second flare, observed only with *NuSTAR*, we had even more limited information. From the analysis of the FPM A and B spectra from the flare interval as a whole and from the rise plus peak segments we derived a plasma temperature of about 5 keV (90% confidence level: 4.3–6.5 keV) and a $N_{\rm H} \sim 1.2 \times 10^{23}$ (0.8–1.7 $\times 10^{23}$) cm^{-2}. The estimate of $N_{\rm H}$ is less precise than that inferred from *XMM-Newton* spectra as the band below 3.0 keV is not observed by *NuSTAR*. However, in agreement with the first flare and its previous flares, this second flare of Elias 29 showed once again a $N_{\rm H}$ value higher than that measured during the quiescence. We discuss this finding in Sect. 4 speculating about the location of the flaring regions in Elias 29.

3.3. NuSTAR *spectroscopy*

In Fig. 9 we show the time averaged *NuSTAR* spectra of the FPMA and FPMB instruments in three different time intervals. The spectra refer to the total exposure, the sum of the quiescent intervals, and the sum of the flaring intervals recorded in *NuSTAR* data. We obtained about 4200 net counts in the total spectra, about 2400 net counts in the quiescent spectra, and about 2000 net counts in the flare spectra. We plot also a best-fit model where, in this case, we added a power law to the APEC+Gaussian model for modeling the spectra above ∼10 keV. Because of the limited count statistics and energy resolution of *NuSTAR* FPM instruments, a free centroid of the Gaussian line does not improve the model results and thus we kept fixed the line centroid at 6.4 keV. A good fit with a model

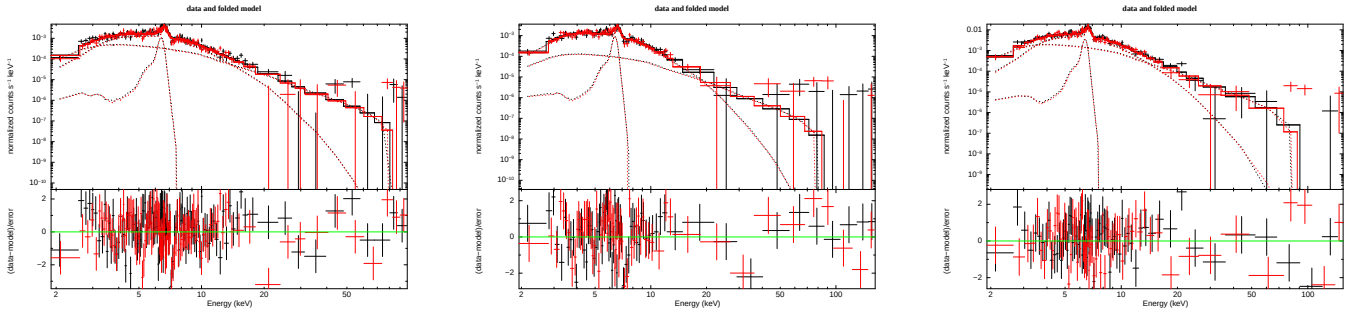

Fig. 9. *NuSTAR* FPM A and B spectra in three different time intervals. Black indicates FPMA, red indicates FPMB. The best-fit models (dashed lines) and the χ^2 terms in units of σ (*bottom panels*) are also shown. *Left panel*: average *NuSTAR* spectra accumulated on the total exposure (≈260 ks). *Central panel*: spectra during the quiescent phase. Right panel: Spectra during the two flares.

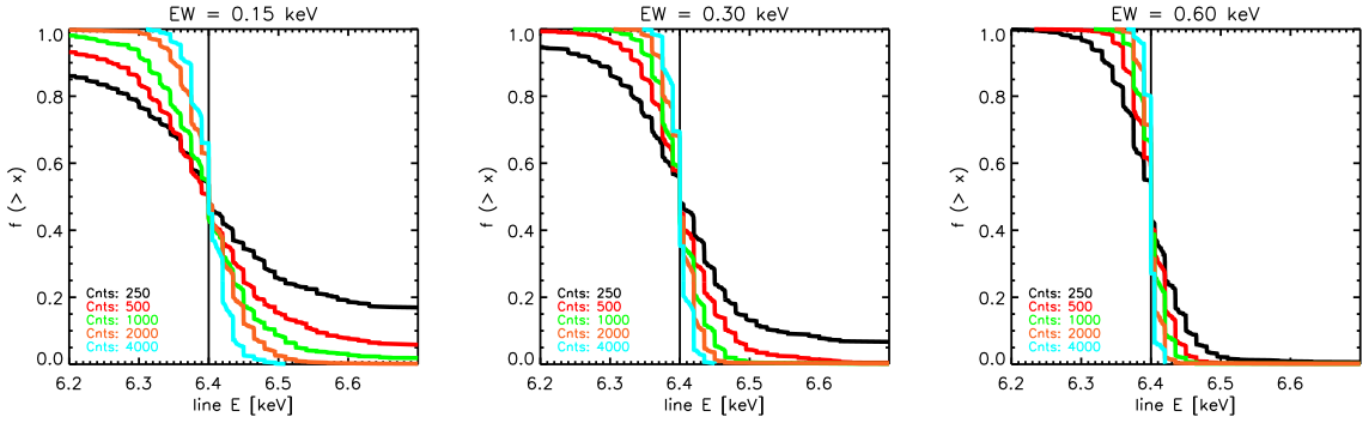

Fig. 10. Cumulative distributions of the best-fit centroid positions of the Gaussian line from the simulations at various levels of count statistics (values in the plots) and for three values of the EW of the Gaussian line used in the starting model (indicated in the title of the plots).

composed by a thermal APEC component and a Gaussian line is satisfactory up to ∼20 keV. A joint fit of *NuSTAR* and PN spectra found a temperature similar to that found with the best fit to the PN spectrum alone. At energies above 20 keV a systematic residual emission is observed in excess of the thermal emission. The spectrum has a low statistics in this spectral range, nevertheless the excess is significant above 2σ and represents to date the best example of hard X-ray spectrum of a YSOs. Adding a second APEC or a Bremsstrahlung components does not improve the fit above 30 keV as evaluated with the χ^2 statistics. Adding a power-law component improves the fit and gives a spectral index $\gamma \sim 1.5-2$ in the energy band ∼20−80 keV. However, the low count statistics above 50 keV after background subtraction makes the best-fit procedure and the χ^2 test not applicable in the 50−80 keV range. We speculate that the emission in 20−50 keV and modeled with a power law could be of non-thermal nature from a population of high energy particles that can contribute to pumping up the fluorescent emission as discussed by Emslie et al. (1986) for energetic solar flares.

The excess of hard X-ray emission with respect to the thermal emission is detected not only during the flare but also during the quiescent phase. This means that the non-thermal component is weak but present also during the quiescent phase rather than being emitted exclusively during the flare. The flux in 10−80 keV varies in 1.8×10^{-13}–3.5×10^{-13} erg s^{-1} cm^{-2} between the quiescent and flaring phases.

3.4. Fluorescent emission

Table A.3 reports the values of the centroids, EWs, and fluxes of the Gaussian line for the fluorescent emission at ∼6.4 keV. We used only the band 5–8 keV as described in Sect. 2 to better determine the centroid and the strength of the Gaussian line. Fluorescence from cold Fe is present in the spectra of Elias 29 in quiescent and flaring states as detected before by Giardino et al. (2007) and Favata et al. (2005) and it is variable in strength and in centroid position. The spectral region in ∼6.4−7 keV is rich in Kα and Kβ lines from neutral to multiply ionized Fe (see Kallman et al. 2004). In a few cases the centroid is at 6.5 keV with a 90% confidence range of ∼6.4−6.7 keV and this can be explained by emission from Fe at higher ionization stages (cf. Emslie et al. 1986).

In order to test the robustness of the centroid determination, we made several sets of simulations of spectra at various levels of count statistics. The spectra are generated from a model composed by a thermal APEC component at 4 keV absorbed by a gas column density of $N_{\rm H} = 5.5 \times 10^{22}$ cm^{-2}, with a global abundance $Z \sim 0.5\,Z_{\odot}$ and a Gaussian line at 6.4 keV with EW in the set: 0, 0.15, 0.3, 0.6, and 0.8 keV. The abundance was kept fixed in one set of 1000 simulations and variable in another set of 1000 simulations. Figure 10 shows the cumulative distributions of the line centroid as a function of the count statistics of the input spectra and various line intensities. From these simulations we infer that in the case of spectra with more than 500 counts and with EW ≥ 0.3 keV there is a very low probability ($P < 0.05$) to determine the centroid at energies well above 6.5 keV. In the data, the most significant case for which we measure the centroid at 6.51 keV before the flare (second *XMM-Newton* exposure, segment 1) is when the number of counts in the spectra are 476, 76, and 50 for PN, MOS1, and MOS2, respectively, and the EW is about 0.47 keV (with a 90% confidence range of 0.25–0.8 keV). We may have caught fluorescent emission from

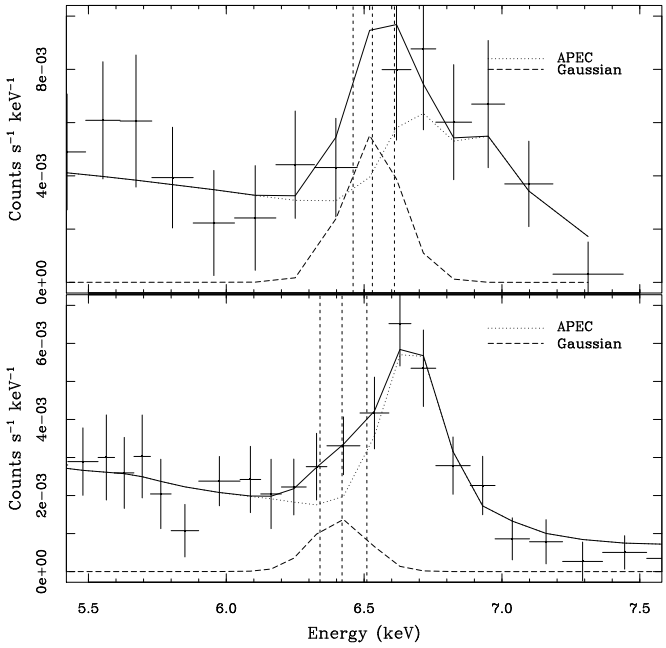

Fig. 11. *Top panel*: PN spectrum and best-fit model (solid line) during segment 1 of the second *XMM-Newton* exposure. Dotted lines show the APEC component; dashed lines show the Gaussian component. *Bottom panel*: same plot for the PN spectrum during the third *XMM-Newton* exposure. Vertical dashed lines in both panels indicate the centroid positions and the 90% confidence range.

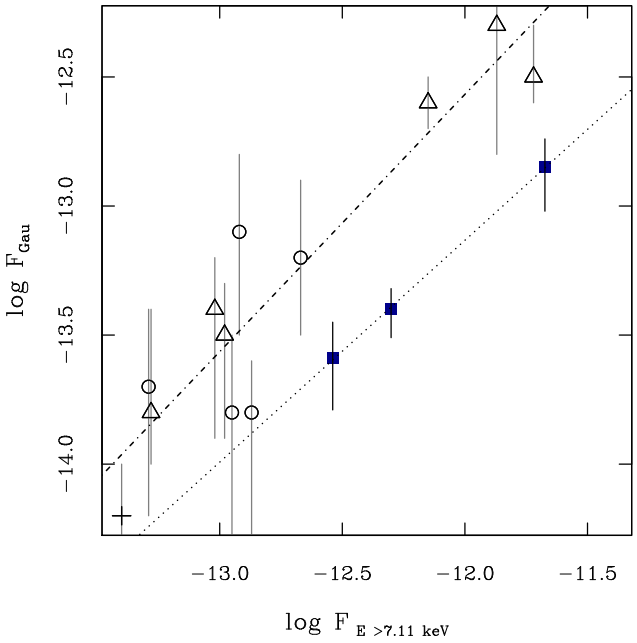

Fig. 12. Flux of the Gaussian spectral component vs. the flux above 7.11 keV. The circles refer to the first *XMM-Newton* observation, the triangles refer to during the flare (triangles), and the cross indicates the last *XMM-Newton* observation. The filled symbols refer to the fluxes derived from *NuSTAR* best-fit models (see Table A.2). The lines are the linear best fit to the *XMM-Newton* and *NuSTAR* data, respectively.

partially ionized Fe just at the beginning of the flare. Figure 11 shows the PN spectra during segment 1 of the second *XMM-Newton* exposure and third exposure. The best-fit model is shown and the centroid in one case is found at ∼6.53 keV and in another case is found at ∼6.42 keV. These values are marginally compatible at the 90% significance level as determined from the uncertainties calculated with XSPEC. Our simulations suggest that these two values of the centroid are different at a 95% significance level given the counts of the spectra are ≥500.

There is marginally significant variability of the line EW during the quiescent intervals just before the first flare, and the other quiescent phases during the first and third *XMM-Newton* observations in absence of evident flaring activity. The EW is found to be between ∼0.15 and ∼0.47 keV.

On the other hand, the flux of the Gaussian line increased when the overall X-ray flux increased. In particular there is a correlation between the flux above 7.11 keV and the flux of the line. In Fig. 12 we show a scatter plot of the flux of the Gaussian line versus the flux above 7.11 keV. In details, we calculated the fluxes in the 7.11–10.0 keV band for the *XMM-Newton* spectra with best-fit parameters in Table A.1 and in the 7.11–80.0 keV band for the *NuSTAR* spectra with best-fit parameters in Table A.2. A systematic excess of the *NuSTAR* fluxes in the 7.11–80.0 keV band is present with respect to the 7.11–10.0 keV *XMM-Newton* fluxes due to the larger bandwidth of *NuSTAR* fluxes. A linear fit between the two fluxes gives a slope of 0.97 ± 0.13 and intercept of -1 ± 1.6. Fitting a relationship of the type $y = Ax$ gives a slope of 1.044 ± 0.005. The three *NuSTAR* points gives a slope of 0.86 ± 0.02 and 1.09 ± 0.005 when fitting without intercept. The correlation between Gaussian flux and flux above 7.11 keV can be understood by the fact that the photons at energies above 7.11 keV can induce Fe fluorescence. However, it is presumable that very hard X-ray photons are not absorbed by material with $N_{\rm H} < 10^{24}$ cm^{-2}, thus the photons that concur to excite fluorescence have energies well below 80 keV.

4. Discussion

Fluorescent emission is a feature of Elias 29 in both the quiescent and flaring states. An EW in excess of 0.15 keV is detected in almost all the time intervals. This result makes a simple model made of an irradiated disk unrealistic and suggests that other mechanisms of reverberation or a more complex geometry that take into account the cavity where Elias 29 sits can have a role in explaining such high EWs. Fe fluorescence in YSOs of ONC has been investigated by Czesla & Schmitt (2010); they remarked how explaining the origin of the fluorescent line at 6.4 keV in a few case of quiescent sources is still an open issue. Their sample of COUP sources spans a range of $N_{\rm H}$ in $2 \times 10^{20} - 2 \times 10^{23}$ cm^{-2} and EWs between ∼0.1 and 0.8 keV (including the quoted uncertainties); the only exception is V 1486 Ori (COUP # 331), which showed EW ≥ 1.4 keV.

In *NuSTAR* spectra we detected an excess of hard X-ray emission in Elias 29 that is likely of non-thermal origin. The counting statistics does not allow us to perform a time-resolved analysis in depth, yet there is no evidence of an increase or a concentration of such a hard emission during flares only because the hard X-ray emission seems produced ubiquitously during the entire observation. We speculate that the excess of hard X-ray emission is associated with a population of accelerated particles moving along the accretion streams and varying with stochastic frequency in time due to a highly structured magnetic field. The average strength of the magnetic field is expected to be on the order of a few hundreds of Gauss to constrain plasma at an average temperature of a few kilo electron-Volts, while, in comparison, the average coronal field in the Sun is on the order of 2 G. Locally the magnetic field of YSOs like Elias 29 can reach

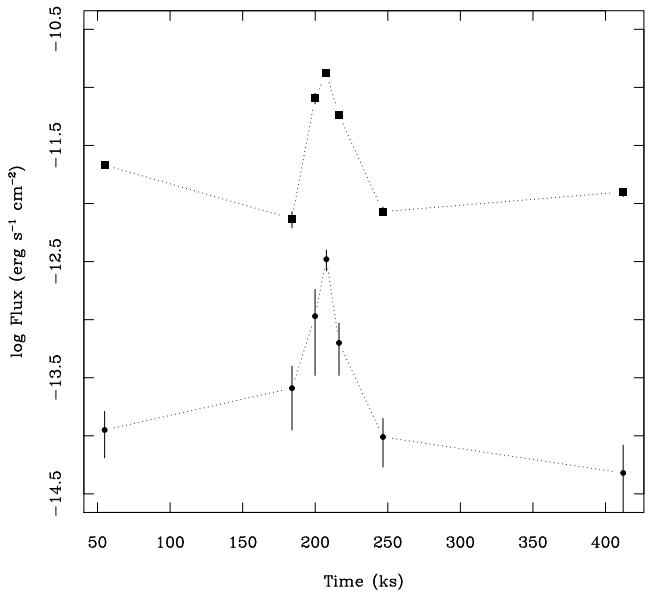

Fig. 13. Flux of the APEC thermal component (large symbols) and the Gaussian line (small dots) as functions of time Error bars refer to 90% significance level of uncertainty.

up to few kilo Gauss of strength in the core of active regions and during flares. Still, it is possible to use the Sun as a template for the corona to build up magnetic fields with values in excess of a kilo Gauss (see Orlando et al. 2003). In such a scenario part of the flux of the Fe Kα 6.4 keV line could originate from collisions of these particles with the disk and a correlation with the intensity of the fluorescence and the non-thermal emission would be expected.

However, a clear correlation between the flux of the thermal component and the flux of the Gaussian line that models the fluorescent emission is still observed during flares. In Fig. 13 we plot the flux of the Gaussian line and the flux of the APEC component as a function of time. During the flare we observe an increase of both fluxes. We interpret this behavior as the increase of fluorescence during the flare due to photons with energies above 7.11 keV. Before and after the flare the value of the flux of the Gaussian line shows very little variation at the 90% significance level. Still, the origin of fluorescence outside the flares remains puzzling when the origin of the phenomenon is explained only in terms of high energy photons because EWs > 0.15 keV seem difficult to obtain with a simple irradiated disk model. In the Sun, Parmar et al. (1984) found that the fluorescence observed during solar flares is produced almost exclusively by photons at $E > 7.11$ keV, while there is very little evidence of electron induced fluorescence in the flares they analyzed. High energy electrons are efficient at stimulating fluorescence when their energies are <25 keV, whereas the efficiency of hard X-ray photons to stimulated fluorescence has a cut off at around 20 keV. With the data in hand we cannot detect any delay between the increase of the fluorescence with respect to the overall coronal flux during the flare. In principle, a delay can be expected if the emitting region is the inner disk and the excitation of the fluorescence takes some time to reach its maximum and to fade out after the flare.

We find a suggestion that the centroid of the fluorescent line could vary in time. From our simulations we estimate a significance of such variation at a 95% confidence level. The change of line centroid can be explained in a scenario in which the emission arises from excited material at various ionization stages whose relative contributions (and associated energy of excited emission lines) to the overall emission in the 6.4−6.6 keV energy band vary with time. Future missions such as Athena (Nandra et al. 2013; Sciortino et al. 2013) provide both a collecting area larger than *XMM-Newton* and high spectral resolution (2.5−3 eV up to 7 keV, Barret et al. 2016). In this respect, Elias 29 appears to be the most promising candidate among Class I YSOs given its proximity. However for observations in the *NuSTAR* band, its weak hard X-ray flux remains still too faint to allow for a more detailed time-resolved analysis.

Isola et al. (2007) found a significant correlation between the soft X-ray emission in the GOES band 1.6−12.4 keV (mostly of thermal nature) and the hard X-ray emission in the RHESSI bands 20−40 keV and 60−80 keV (mostly of non-thermal nature) during solar flares. This correlation holds up to the most energetic events, spanning about four orders of magnitude in peak flux. These authors showed that the same scaling law holds for the handful of available hard X-ray observations of intense stellar flares observed with Beppo*SAX* in active stellar binaries or zero-age main sequence stars. If the X-ray emission in Class I/II YSOs is just a scaling up of solar phenomena, we expect such a correlation to be valid for very young pre-main sequence stars. In Elias 29 the flux at the peak of the flare from the PN spectrum of segment 3 in the 1.6−12.4 keV band is $F_S = 1.8 \times 10^{-14}$ W m^{-2}; from the *NuSTAR* spectrum of the whole flare the flux in 20−40 keV is 1.16×10^{-13} erg s^{-1} cm^{-2} corresponding to $F_H = 5.0 \times 10^{-7}$ photons cm^{-2} s^{-1} keV^{-1}. For a direct comparison to the Isola et al. (2007) results we rescaled these two quantities to a distance of 1 AU obtaining a flux of $F_S \approx 10.97$ W m^{-2} (1.6–12.4 keV band) and $F_H \sim 305 \times 10^6$ photons cm^{-2} s^{-1} keV^{-1} (20–40 keV band). The relationship of Isola et al. predicts $F_S \sim 12.22$ W m^{-2}, which is within a 10% of uncertainty from our measurement of F_S. It is evinced that in a Class I object such as Elias 29 the soft and hard fluxes at the flares show the same scaling law empirically found for the Sun and active stars. The flare of Elias 29 can be considered a scaled-up version of powerful solar flares and similar to those of active stars on the main sequence.

A further test for the analogy between the flare in Elias 29 and the solar flares was based on the thermal flux estimated by Isola et al. (2007). We used the flux in the 20−40 keV band measured from *NuSTAR* spectra and the coefficient of scaling m given in Table A.2 of Isola et al. (2007) and corresponding to the temperature of 6 keV (the closest to that observed in Elias 29) to estimate the thermal flux in the 1.6−12.4 keV band.; we compared this flux to that observed in our PN spectrum. The flux we obtain is $F_S \sim 1.8 \times 10^{-14} * m = 6.51 \times 10^{-7}$ to be compared to 5.0×10^{-7} photons cm^{-2} s^{-1} keV^{-1}, which is within 30% uncertainty from the value estimated from Isola et al. relationship. This again corroborates the analogy between the flare of a very young corona of a Class I object (Elias 29) and the flares of more evolved active stars.

The Coordinated Synoptic Observations (CSI) observed the YSOs in the ~3 Myr old NGC 2264 SFR simultaneously with *C*OROT, *Chandra*, and *S*pitzer. Light curves of tens of Class I, II, and III YSOs were obtained during the ~3.5 days CSI campaign and several tens of flares were detected. Flaccomio et al. (2018) showed that the energy released during some of such flares, E_{flare}, can easily reach values up to $\sim 10^{36}$ erg, i.e., up to 1–2 dex above the energy released in the strongest (X100 class) flares ever observed on the Sun. The flare in Elias 29 released an energy of about 8×10^{34} erg and this is in the median of the energies of the detected flares in NGC 2264. At the same level of flare energy from studies on other SFRs like ONC

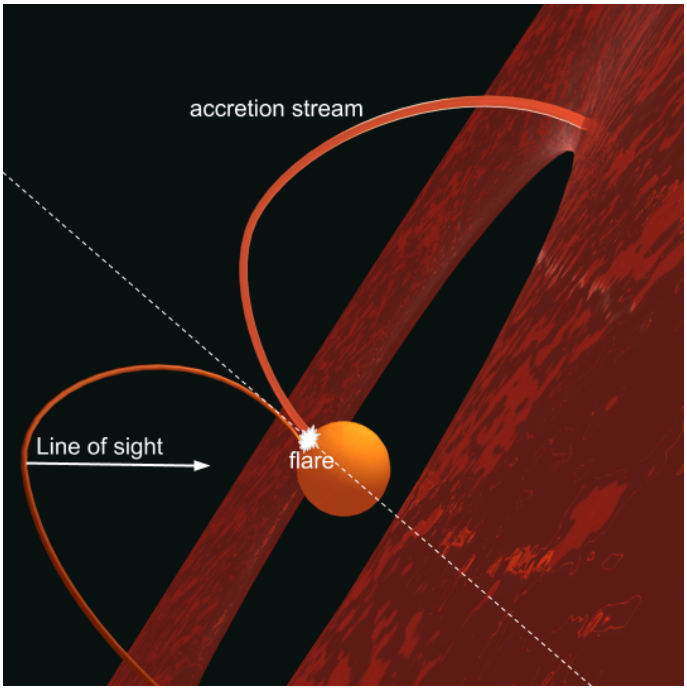

Fig. 14. Cartoon of the proposed scenario to explain the increase of $N_{\rm H}$ during flares. The flares originate at the base of the accretion stream located around the pole and, in a face-on geometry, the emitted X-rays would cross a portion of the accretion stream with $N_{\rm H}$ absorption larger than the average $N_{\rm H}$ value.

(Caramazza et al. 2007) and Cyg OB2 (Albacete Colombo et al. 2007), a frequency of flares of about $1-2\,{\rm Ms}^{-1}$ is expected. When also considering the DROXO exposure, Elias 29 showed two similar flares detected in a global *XMM-Newton* exposure of 800 ks, which is in good agreement with the flaring rate derived in other SFR regions.

The energy released during the flare is high even when compared to the energies released by the most powerful solar flares, but it is on the same order of magnitude of the energies of flares of similar YSOs. On the other hand, the peak temperature is very high on top of an already hot temperature during quiescence (130 MK versus ~50 MK). A flare with similar duration was also observed in DROXO (Giardino et al. 2007). A compact size of the hosting loop(s) is suggested.

A peculiar feature of the flares in Elias 29 is the increase of gas absorption of about five times during the flares as described in Sect. 3.2.3. The increase of gas absorption was also observed in past flares observed with *XMM-Newton* and ASCA (Giardino et al. 2007; Kamata et al. 1997). Kamata et al. (1997) speculated that, under the hypothesis that the disk is edge on, the flares occur at low latitudes and the X-rays pass through the disk being thus heavily absorbed, while the X-rays emitted during quiescent phases are coming from the rest of the corona and encounter less gas along the line of sight. However, while plausible, this interpretation conflicts with the geometry of the source extrapolated from submillimeter and far-infrared observations (e.g., Boogert et al. 2002; Ceccarelli et al. 2002; Miotello et al. 2014; Rocha & Pilling 2015, see also Fig. 14). An alternative explanation that can reconcile the system geometry and the higher gas absorption during flares is that the flares are generated near the feet of the accretion streams (see Fig. 14). The feet could be located preferentially at high stellar latitudes around the stellar poles as the streams follow the large-scale dipolar geometry of the magnetic field and likely these are the sites of frequent flares. The X-rays generated during the flares at the stream feet travel a portion of the path across the dense accreting gas before arriving to the observer. As a result the gas absorption measured during flares is found to be systematically larger than that measured from the quiescent corona.

Finally, a different scenario can in principle explain both the $N_{\rm H}$ enhancement associated with flares and the large EW observed for the 6.4 keV line. Elias 29 displays a hard X-ray emission ($E > 20$ keV), possibly of non-thermal origin, in addition to its thermal X-ray spectrum ($E < 20$ keV) of the corona. At these energies the number of X-ray photons that undergo Compton scattering, instead of photo-absorption, could be non-negligible. Compton scattering diminishes the energy of scattered photons and causes a global softening of the X-ray spectrum. Depending on the system geometry, Compton scattering could therefore mimic a $N_{\rm H}$ lower than that experienced by the primary X-ray photons emitted by the corona on our line of sight. In fact, the line of sight toward Elias 29 passes approximately on the edge of the inner cavity. Therefore X-ray photons scattered toward us by the disk surface and the inner cavity wall experience an $N_{\rm H}$ lower than that suffered by primary photons emitted by the central star. Hence, the total X-ray spectrum reaching us would be approximately composed of highly absorbed primary X-ray photons and less-absorbed scattered photons. In this scenario, an increase of the thermal emission of the corona (i.e., a flare) implies an increase of the highly absorbed primary-photon component only. That would therefore explain why the X-ray flares observed on Elias 29 show $N_{\rm H}$ systematically higher than that of the quiescent phases. In addition, assuming that the real $N_{\rm H}$ between us and the central star is that observed during flares (i.e., $\sim 2\times10^{23}\,{\rm cm}^{-2}$), the EW of the fluorescent line at 6.4 keV is larger than the model predictions; this is simply because, at these $N_{\rm H}$ values, photons at ~7.1 keV start to be significantly absorbed, while the fluorescent line, originating preferentially from the disk surface and the inner cavity wall, is less absorbed. Such a scenario is qualitatively similar to that of AGNs, where the EW of the 6.4 keV line is observed to increase up to values of ~1 keV for increasing $N_{\rm H}$ (e.g., Fukazawa et al. 2011). The case of Elias 29, i.e., EW $\sim$ 0.3 keV and $N_{\rm H} \sim 10^{23}\,{\rm cm}^{-2}$, would neatly fit the EW versus $N_{\rm H}$ pattern observed in AGNs.

5. Summary

We presented the results of a joint *XMM-Newton* and *NuSTAR* simultaneous observation of Elias 29, which is the IR brightest Class I object in the Rho Ophiuchi Dark Cloud core F (LDN 1688). The full EPIC image contains about 100 X-ray sources, while *NuSTAR* shows about ten sources among which Elias 29 is the brightest. We observed a flare of duration of about 20 ks with a regular exponential-like decay characterized by an e-folding time of about 7.6 ks in the 0.3–5.0 keV band and a rise time of about 3 ks. Through time-resolved spectroscopy we inferred the properties of the quiescent and the flaring plasma. We determined that the flaring structures are relatively compact with a length of about $1-2\,R_{\odot}$, which suggests that likely the loop is anchored to the stellar surface. A magnetic field of at least 500 G is required to confine the plasma within the loop. A second flare with a duration of 50 ks was observed with *NuSTAR* only and for which we inferred a loop size similar to that that hosted the first flare. During these flares we observed an increase of $N_{\rm H}$ that suggests a specific location of the flaring sites at the base of the accretion streams of the star.

Fluorescent emission from neutral or partially ionized Fe is observed both during quiescence and during the flares. Fluorescence is modeled with a Gaussian line varying both in the centroid position and in strength. There is a clear correlation between fluorescent emission and coronal emission during the flare. However, there is still significant Fe fluorescence outside the flare that cannot be explained exclusively with the contribution of photons at $E > 7.11$ keV. We detect a hard X-ray emission from Elias 29 above ~20 keV, which is not explained by a thermal emission. We argue that a non-thermal population of electrons accelerated from the coronal magnetic field could be responsible for this emission. We speculate that the same population could contribute to the fluorescent emission of Elias 29.

Acknowledgements. We thank the anonymous referee for her/his comments and suggestions which improved the manuscript. The authors acknowledge modest financial contribution from the agreement ASI-INAF n.2017-14.H.O. IP acknowledges support from the ASI and the Ariel Consortium. We made use of *R*, a language and environment for statistical computing, the XMM-SAS suite, HEASOFT fv, XSPEC and DS9.

References

Albacete Colombo, J. F., Caramazza, M., Flaccomio, E., Micela, G., & Sciortino, S. 2007, A&A, 474, 495
Ballantyne, D. R., & Fabian, A. C. 2003, ApJ, 592, 1089
Ballantyne, D. R., Fabian, A. C., & Ross, R. R. 2002, MNRAS, 329, L67
Barret, D., Lam Trong, T., den Herder, J.-W., et al. 2016, in Space Telescopes and Instrumentation 2016: Ultraviolet to Gamma Ray, Proc. SPIE, 9905, 99052F
Bontemps, S., André, P., Kaas, A. A., et al. 2001, A&A, 372, 173
Boogert, A. C. A., Hogerheijde, M. R., Ceccarelli, C., et al. 2002, ApJ, 570, 708
Caramazza, M., Flaccomio, E., Micela, G., et al. 2007, A&A, 471, 645
Ceccarelli, C., Boogert, A. C. A., Tielens, A. G. G. M., et al. 2002, A&A, 395, 863
Czesla, S., & Schmitt, J. H. H. M. 2007, A&A, 470, L13
Czesla, S., & Schmitt, J. H. M. M. 2010, A&A, 520, A38
Drake, J. J., Ercolano, B., & Swartz, D. A. 2008, ApJ, 678, 385
Emslie, A. G., Phillips, K. J. H., & Dennis, B. R. 1986, Sol. Phys., 103, 89
Erdman, C., & Emerson, J. W. 2007, J. Stat. Softw., 23, 1
Erdman, C., & Emerson, J. W. 2008, Bioinformatics, 24, 2143
Favata, F., & Micela, G. 2003, Space Sci. Rev., 108, 577
Favata, F., Flaccomio, E., Reale, F., et al. 2005, ApJS, 160, 469
Feigelson, E. D., & Montmerle, T. 1999, ARA&A, 37, 363
Flaccomio, E., Micela, G., Sciortino, S., et al. 2005, ApJS, 160, 450
Flaccomio, E., Micela, G., Sciortino, S., & CSI Collaboration. 2018, A&A, 620, A55
Fukazawa, Y., Hiragi, K., Mizuno, M., et al. 2011, ApJ, 727, 19
Getman, K. V., Flaccomio, E., Broos, P. S., et al. 2005, ApJS, 160, 319
Giardino, G., Favata, F., Pillitteri, I., et al. 2007, A&A, 475, 891
Golub, L., Maxson, C., Rosner, R., Vaiana, G. S., & Serio, S. 1980, ApJ, 238, 343
Güdel, M. 2003, Adv. Space Res., 32, 2045
Güdel, M., & Telleschi, A. 2007, A&A, 474, L25
Güdel, M., Briggs, K. R., Arzner, K., et al. 2007, A&A, 468, 353
Harrison, F. A., Craig, W. W., Christensen, F. E., et al. 2013, ApJ, 770, 103
Imanishi, K., Koyama, K., & Tsuboi, Y. 2001, ApJ, 557, 747
Isola, C., Favata, F., Micela, G., & Hudson, H. S. 2007, A&A, 472, 261
Kallman, T. R., Palmeri, P., Bautista, M. A., Mendoza, C., & Krolik, J. H. 2004, ApJS, 155, 675
Kamata, Y., Koyama, K., Tsuboi, Y., & Yamauchi, S. 1997, PASJ, 49, 461
Kastner, J. H., Huenemoerder, D. P., Schulz, N. S., Canizares, C. R., & Weintraub, D. A. 2002, ApJ, 567, 434
Killick, R., Fearnhead, P., & Eckley, I. A. 2012, J. Am. Stat. Assoc., 107, 1590
Klimchuk, J. A., Antiochos, S. K., Norton, D., & Watko, J. A. 2000, AAS/Solar Physics Division Meeting, 31, 01.44
Maggio, A., Pallavicini, R., Reale, F., & Tagliaferri, G. 2000, A&A, 356, 627
Maggio, A., Flaccomio, E., Favata, F., et al. 2007, ApJ, 660, 1462
Miotello, A., Testi, L., Lodato, G., et al. 2014, A&A, 567, A32
Montmerle, T. 1990, in Rev. Mod. Astron., ed. G. Klare, 3, 209
Nandra, K., Barret, D., Barcons, X., et al. 2013, ArXiv e-prints [arXiv:1306.2307]
Natta, A., Testi, L., & Randich, S. 2006, A&A, 452, 245
Orlando, S., Peres, G., & Reale, F. 2003, Adv. Space Res., 32, 955
Parmar, A. N., Culhane, J. L., Rapley, C. G., et al. 1984, ApJ, 279, 866
Pillitteri, I., Sciortino, S., Flaccomio, E., et al. 2010, A&A, 519, A34
Reale, F. 2007, A&A, 471, 271
Reale, F. 2014, Living Rev. Sol. Phys., 11, 4
Rocha, W. R. M., & Pilling, S. 2015, ApJ, 803, 18
Sciortino, S., Rauw, G., Audard, M., et al. 2013, ArXiv e-prints [arXiv:1306.2333]
Stelzer, B., Flaccomio, E., Pillitteri, I., Argiroffi, C., & Sciortino, S. 2011, in 16th Cambridge Workshop on Cool Stars, Stellar Systems, and the Sun, eds. C. Johns-Krull, M. K. Browning, & A. A. West, ASP Conf. Ser., 448, 1279
Townsley, L. K., Broos, P. S., Corcoran, M. F., et al. 2011, ApJS, 194, 1
Tsuboi, Y., Yamazaki, K., Sugawara, Y., et al. 2016, PASJ, 68, 90
Tsujimoto, M., Feigelson, E. D., Grosso, N., et al. 2005, ApJS, 160, 503
Wang, X., & Emerson, J.W. 2015, Working Paper
Wolk, S. J., Harnden, Jr., F. R., Flaccomio, E., et al. 2005, ApJS, 160, 423

Appendix A: Tables

Table A.1. Parameters from best-fit model in the spectra from the time intervals identified with the PELT algorithm (Fig. 4).

Obs	Segment	Counts	N_H (10^{22} cm^{-2})	kT (keV)	log EM (cm^{-3})	log Flux (erg s^{-1} cm^{-2})	log L_X (erg s^{-1})	Centroid (keV)	log F_{Gau} (erg s^{-1} cm^{-2})	EW (keV)	log $F_{E>7.11\,keV}$ (erg s^{-1} cm^{-2})	χ^2_{red}	Prob	D.o.F.
First	1	2049+200+190	7.2 (4.8–11)	4 (2.3–8.6)	53.24 (53.18–53.28)	−11.81 (−12 – −11.48)	30.43	6.63 (6.49–6.75)	−13.1 (−13.72 – −12.94)	0.21	−12.92	1.07	0.3	91
	2	2317+662+851	7.2 (6.6–7.9)	4.2 (3.5–5)	53.32 (53.28–53.33)	−11.73 (−11.79 – −11.67)	30.51	6.48 (6.42–6.55)	−13.73 (−14.03 – −13.56)	0.23	−12.87	1.14	0.14	131
	3	1225+369+500	6.4 (5.8–7.12)	5.4 (4.2–6.9)	53.35 (53.32–53.36)	−11.67 (−11.7 – −11.61)	30.57	6.57 (6.51–6.63)	−13.31 (−13.57 – −13.14)	0.23	−12.67	0.99	0.48	75
	4	1074+314+464	6.3 (5.6–7.1)	3.4 (3–4.4)	53.35 (53.32–53.38)	−11.72 (−11.79 – −11.65)	30.52	6.31 (5.97–6.5)	−13.87 (−14.82 – −13.6)	0.19	−12.95	1.54	0.003	67
	5	962+250+401	5.4 (4.4–6.2)	5.4 (3.8–14.1)	53.03 (53–53.05)	−11.99 (−12.11 – −11.9)	30.25	6.57 (6.5–6.63)	−13.56 (−13.85 – −13.28)	0.28	−13.29	1.9	4e-05	59
Second	1	1800+389+351	9 (6.8–12.4)	3.9 (2.6–6.3)	53.12 (53.08–53.15)	−11.94 (−12.09 – −11.7)	30.30	6.49 (6.4–6.57)	−13.62 (−13.96 – −13.42)	0.51	−12.98	1.15	0.15	91
	2	534+141+193	21.3 (15.9–27.2)	11.1 (5.2–64)	54 (53.95–54.04)	−11.06 (−11.16 – −10.78)	31.18	6.6 (6.38–6.66)	−12.44 (−13.23 – −12.21)	0.3	−11.87	1.36	0.1	27
	3	1842+583+660	19.9 (18.4–21.5)	6.9 (5.4–6.8)	54.24 (54.22–54.28)	−10.69 (−10.74 – −10.65)	31.55	6.4 (6.38–6.43)	−12.39 (−12.49– −12.3)	0.36	−11.72	1.65	7e-05	91
	4	952+355+371	15.6 (14.2–17.3)	5.5 (4.5–7.9)	53.79 (53.77–53.82)	−11.22 (−11.36 – −11.15)	31.02	6.5 (6.59–6.45)	−12.85 (−13.01 – −12.72)	0.59	−12.15	1.39	0.028	55
	1 and 5	2919+707+714	7 (6.1–7.9)	5.9 (4.9–8.7)	52.82 (52.8–52.84)	−12.19 (−12.37 – −12.14)	30.05	6.51 (6.46–6.58)	−13.73 (−13.88 – −13.6)	0.51	−13.02	1.22	0.04	137
	5	1455+472+509	7.2 (6.4–8.1)	3.6 (3.1–4.3)	52.94 (52.92–52.96)	−12.16 (−12.24 – −12.09)	30.08	6.56 (6.49–6.61)	−13.71 (−13.89 – −13.57)	0.56	−13.28	1.36	0.015	86
Third	1	2040+685+782	5.5 (5.02–6.37)	4.2 (3.5–5.6)	52.78 (52.77–52.79)	−12.22 (−12.3 – −12.17)	30.02	6.42 (6.34–6.51)	−14.31 (−14.84 – −14.08)	0.19	−13.4	1.2	0.062	127
	Quiesc	3391	5.8 (5.3–6.4)	4.2 (3.6–5.3)	52.82 (52.75–52.89)	−12.21 (−12.23 – −12.20)	30.03	6.49 (6.40–6.60)	−14.17 (−14.41 – −14.02)	0.25 (0.16–0.38)	−13.15	1.1	0.21	127

Notes. The model is an absorbed APEC thermal component plus a Gaussian that models the fluorescence at ∼6.4−6.6 keV. Ranges at the 90% confidence level are indicated in braces, and in some cases the high limit of temperature uncertainty is not constrained. A value of $Z/Z_\odot$ of 0.54 has been derived from the third exposure (quiescent phase) and used for the best fit of the spectra of the first and second exposures. The 90% confidence level uncertainty of the EWs of the Gaussian line is on the order of 0.1–0.3 keV. Unabsorbed fluxes for the APEC and the Gaussian components are given in the energy band 0.3–8.0 keV, the fluxes at $E > 7.11$ keV are also listed. X-ray luminosities are calculated from fluxes using a distance of 120 pc.

Table A.2. Parameters of the best-fit models to the *NuSTAR* spectra shown in Fig. 9.

Spectrum	N_H (10^{22} cm^{-2})	kT (keV)	$Z/Z_\odot$	log EM (cm^{-3})	γ	EW (keV)	log $F_{20-40\,keV}$ (erg s^{-1} cm^{-2})	log $F_{7.11-80\,keV}$ (erg s^{-1} cm^{-2})
Total	14.1 (8.9–20.7)	3.9 (3.2–4.7)	0.53 (0.42–0.66)	53.4 (53.27–53.57)	2.1 (1.7–2.3)	0.34 (0.25–0.49)	−13.04	−12.29
Quiescent	8.8 (5.3–14.8)	3.6 (2.8–4.4)	0.53 (NA–NA)	53.3 (53.19–53.47)	2.2 (0.6–2.9)	0.39 (0.27–0.61)	−13.4	−12.55
Flare	19.4 (13.5–26)	4.1 (3.5–4.9)	0.53 (NA–NA)	53.96 (53.85–54.1)	1.9 (1.7–2.2)	0.28 (0.18–0.45)	−12.36	−11.64

Table A.3. Parameters from best-fit model of the spectra in 5.0−8.0 keV band.

Obs	Segment	Counts (PN, MOS1, MOS2)	kT (keV)	EM (cm^{-3})	Z	Centroid (keV)	N_{Gau} (10^{-7} photons cm^{-2} s^{-1})	EW (keV)	F_{APEC} (erg s^{-1} cm^{-2})	F_{Gau} (erg s^{-1} cm^{-2})	χ^2_{red}	Prob
First	All	1716+353+537	3.6 (2.9–4.2)	53.39 (53.28 – 53.52)	0.53 (0.45–0.61)	6.42 (6.38–6.48)	11.4 (6.7–16)	0.15 (0.10–0.2)	−11.67 (−11.7 – −11.66)	−13.95 (−14.19 – −13.79)	1.22	0.11
Second	1	463+76+50	10.8 (3.5–13.4)	52.86 (52.67–53.22)	1 (0.2–5)	6.53 (6.43–6.61)	25 (8.4–44)	0.47 (0.25–0.8)	−12.13 (−12.21 – −12.07)	−13.59 (−13.95 – −13.4)	0.71	0.83
	2	330+50+78	7.9 (5.3–9.1)	53.8 (53.68–53.94)	1.5 (0.9–2.4)	6.51 (6.4–6.7)	160 (62–540)	0.21 (0.10–0.4)	−11.09 (−11.14 – −11.05)	−12.97 (−13.48 – −12.74)	1.05	0.39
	3	1239+230+303	7 (6.3–7.9)	54.02 (53.96–54.08)	1.65 (1.3–2.1)	6.4 (6.37–6.43)	320 (260–390)	0.41 (0.33–0.5)	−10.88 (−10.9 – −10.86)	−12.48 (−12.58 – −12.4)	1.15	0.21
	4	515+128+126	4.8 (3.2–6.7)	53.78 (53.65–53.98)	0.54 (0.35–0.79)	6.48 (6.43–6.58)	93 (55–135)	0.22 (0.15–0.4)	−11.24 (−11.27 – −11.21)	−13.2 (−13.48 – −13.03)	0.69	0.87
	5a	459+75+100	2.1 (1.4–4.1)	53.35 (52.95–53.74)	0.75 (0.1–1.3)	6.33 (6.06–6.6)	6.3 (1.4–26.7)	0.21 (0.11–0.5)	−11.74 (−11.78 – −11.7)	−14.24 (−14.82 – −14)	0.47	0.98
	1 and 5	953+176+152	4.3 (1.9–5.9)	52.95 (52.92–52.99)	0.6 (0.4–0.9)	6.45 (6.4–6.52)	12 (6.5–16)	0.34 (0.23–0.6)	−12.07 (−12.1 – −12.03)	−14.01 (−14.27 – −13.85)	1.13	0.27
Third	All	564+126+125	2.3 (1.5–3.8)	53.28 (52.89–53.71)	0.4 (0.3–0.5)	6.42 (6.34–6.53)	4.9 (1.4–8.5)	0.21 (0.10–0.4)	−11.9 (−11.94 – −11.87)	−14.32 (−14.9 – −14.08)	1.31	0.12

Notes. For the first and third *XMM-Newton* observations we considered the spectra of the full exposure, for the second observation we considered the spectra in the time intervals identified with PELT (see Fig. 4). Uncertainty ranges at 90% confidence level are in reported. Gas absorption has been fixed to $N_H = 5.5 \times 10^{22}$ cm^{-2}. Fluxes of the APEC and the Gaussian components are calculated in the 0.3–8.0 keV band; these fluxes are plotted in Fig. 13 as functions of time.